Stability of a single tunnel in cohesive–frictional soil subjected to surcharge loading

Kentaro Yamamoto, Andrei V. Lyamin, Daniel W. Wilson, Scott W. Sloan, and Andrew J. Abbo

Abstract: This paper focuses mainly on the stability of a square tunnel in cohesive–frictional soils subjected to surcharge loading. Large-size noncircular tunnels are quickly becoming a widespread building technology by virtue of the development of advanced tunneling machines. The stability of square tunnels in cohesive–frictional soils subjected to surcharge loading has been investigated theoretically and numerically, assuming plane strain conditions. Despite the importance of this problem, previous research on the subject is very limited. At present, no generally accepted design or analysis method is available to evaluate the stability of tunnels or openings in cohesive–frictional soils. In this study, a continuous loading is applied to the ground surface, and both smooth and rough interface conditions between the loading and soil are modelled. For a series of tunnel geometries and material properties, rigorous lower and upper bound solutions for the ultimate surcharge loading of the considered soil mass are obtained by applying recently developed numerical limit analysis techniques. The results obtained are presented in the form of dimensionless stability charts for practical convenience, with the actual surcharge loads being closely bracketed from above and below. As a handy practical means, upper bound rigid-block mechanisms for square tunnels have also been developed, and the obtained values of collapse loads were compared with the results from numerical limit analysis to verify the accuracy of both approaches. Finally, an expression that approximates the ultimate surcharge load of cohesive–frictional soils with the inclusion of shallow square tunnels has been devised for use by practicing engineers.

Key words: shallow tunnel, stability, rigid-block mechanism, limit analysis, finite elements.

Résumé : Cet article discute principalement de la stabilité d'un tunnel carré dans des sols cohésifs–frictionnels soumis à des sollicitations en surcharge. Les grands tunnels non circulaires deviennent rapidement une technologie de construction répandue en raison du développement de machines avancées de creusage de tunnels. La stabilité des tunnels carrés dans les sols cohésifs–frictionnels soumis à des sollicitations en surcharge a été étudiée de façon théorique et numérique en supposant des conditions de déformation en plan. Malgré l'importance de ce problème, il y a peu d'études antérieures sur ce sujet. À présent, aucune conception générale n'est acceptée ni méthode d'analyse n'est disponible pour évaluer la stabilité des tunnels ou des ouvertures dans les sols cohésifs–frictionnels. Dans cette étude, une charge est appliquée en continu à la surface du sol et des conditions autant lisses que rugueuses à l'interface entre la charge et le sol sont modélisées. Grâce aux techniques numériques d'analyse limite récemment développées, des solutions rigoureuses à frontière inférieure et supérieure pour la charge en surcharge ultime de la masse de sol considérée sont obtenues, et ce, pour une série de géométries de tunnel et de propriétés de matériaux. Les résultats obtenus sont présentés sous forme de chartes de stabilité sans dimension pour des raisons pratiques, avec les charges de surcharge actuelles étant bien encadrées au-dessus et au-dessous. Des mécanismes de blocs rigides à frontière supérieure pour des tunnels carrés ont aussi été développés comme outil pratique, et les valeurs de charges d'effondrement obtenues ont été comparées avec les résultats de l'analyse limite numérique afin de vérifier la précision des deux approches. Pour terminer, une expression pour obtenir une approximation de la charge de surcharge ultime pour les sols cohésifs–frictionnels avec l'inclusion de tunnels carrés a été développée pour être utilisée par les ingénieurs praticiens.

Mots-clés : tunnel peu profond, stabilité, mécanisme de bloc rigide, analyse limite, éléments finis.

[Traduit par la Rédaction]

Introduction

Accurate assessment of the stability of shallow tunnels, pipelines, and mine workings in cohesive–frictional soils is an important task due to the ubiquitous construction of buildings and tunnels in urban areas and extensive mining explorations caused by the booming demand in natural resources. Since many tunnels and pipelines already exist at deep levels, new tunnels and openings are now often being constructed at shallow depths. In these cases, it is important to know how the stability of these tunnels or openings is affected by surcharge loading. On the other hand, multilevel underground mining technologies require assessment of stability of access

Received 27 July 2010. Accepted 24 August 2011. Published at www.nrcresearchpress.com/cgj on 23 November 2011.

K. Yamamoto. Department of Ocean Civil Engineering, Kagoshima University, Kagoshima 890-0065, Japan.
A.V. Lyamin, D.W. Wilson, S.W. Sloan, and A.J. Abbo. Centre for Geotechnical and Materials Modelling, University of Newcastle, Newcastle, NSW 2308, Australia.

Corresponding author: A.V. Lyamin (e-mail: Andrei.Lyamin@newcastle.edu.au)

ways and extraction zones, in particular, the level under the loads applied from all the top layers, which comes to the same category of stability problems. Unfortunately, there is no generally accepted design or analysis method available to evaluate the ultimate surcharge loading of cohesive–frictional soils that considers the interface conditions between the loading and the soil with a shallow tunnel. The efficient utilization of the underground space dictates that noncircular openings and tunnels should be preferred in the design, as quadrilateral objects such as trains and buildings are usually used there. Furthermore, large-size noncircular tunnels are quickly becoming a widespread building technology by virtue of the development of advanced tunneling machines. The benefits of the construction of noncircular underground openings compared to circular ones would be the reduction of the area of the excavated section, the reduction in surplus soils, thus diminished environmental issues, and the reduction in the size of the rented site for the construction of tunnels. Although the top, bottom, right, and left spaces of circular tunnels are usually useless, circular tunnels have been predominantly used so far, since their construction is easier from the standpoint of excavation and maintenance of the heading. Another important consideration is the high stability numbers of circular tunnels with respect to rectangular geometry due to the arching effect.

The goal of this study is to equip design engineers with simple design tools to determine the stability of square tunnels in cohesive–frictional soils subjected to surcharge loading. Drained loading conditions are considered, the internal tunnel pressure is set to zero, and a continuous load is applied to the ground surface. Both smooth and rough interface conditions between the loading and soil are modelled. For a series of tunnel size to depth ratios and material properties, rigorous lower and upper bound solutions for the ultimate surcharge loading of the soil mass are obtained by applying numerical limit analysis techniques (Lyamin and Sloan 2002; Krabbenhøft et al. 2005). For practical convenience, the results are presented in the form of dimensionless stability charts, with the actual surcharge loads being closely bracketed from above and below. The numerical limit analysis results are verified through comparison with upper bound collapse loads estimated using rigid-block mechanisms postulated for modelling the collapse of square tunnels.

The stability of circular tunnels was studied extensively studied at the University of Cambridge (Cambridge, UK) in the 1970s; see, for example, the work reported by Atkinson and Cairncross (1973), Cairncross (1973), Mair (1979), Seneviratne (1979), and Davis et al. (1980). Later, theoretical solutions for circular tunnel problems were given by Muhlhaus (1985) as well as Leca and Dormieux (1990).

The application of computational limit analysis to the stability of shallow tunnels has been pioneered by Sloan and Assadi who investigated the undrained stability of a plane strain square tunnel in a cohesive soil (Assadi and Sloan 1991) and the stability of square and circular tunnels in a cohesive soil with shear strength varying linearly with depth (Sloan and Assadi 1991, 1992) using linear programming techniques. The stability of the tunnel was described conveniently by two load parameters, $(\sigma_s - \sigma_t)/c_{u0}$ and $\gamma D/c_{u0}$. Here, D is tunnel size, σ_s is surcharge, σ_t is internal tunnel pressure, c_{u0} is undrained shear strength at the ground surface, and γ is soil unit weight. Lyamin and Sloan (2000) and Lyamin et al. (2001) considered stability of plane strain circular and square tunnels in cohesive–frictional soil. The nonlinear programming technique was applied, which vastly reduced the central processing unit (CPU) time required and also allowed for the increase of the number of finite elements employed for the analyses, thus resulting in very accurate solutions. The drained stability of the tunnel was described by the load parameter, σ_t/c'.

Previous studies on the stability of soils with tunnel inclusions have been mainly focused on the stability of tunnels in terms of the allowable internal pressure. This paper extends the work of Yamamoto et al. (2007) in which the ultimate surcharge loading of cohesive–frictional soils with shallow circular and square tunnels beneath the loaded surface was investigated.

Problem description

The surcharge load of the soil with a shallow tunnel is determined by applying a continuous surface loading to the problem domain (Fig. 1). The ground is modelled as a uniform Mohr–Coulomb material with a cohesion c', friction angle ϕ', unit weight γ, and assuming drained loading conditions. The tunnel is of dimension B and depth H, and is modelled with no internal tunnel pressure ($\sigma_t = 0$) that would either resist inward collapse of the tunnel or drive a blowout failure of the tunnel. The ultimate surcharge load of cohesive–frictional soils with inclusion of shallow square tunnels is conveniently described by the dimensionless load parameter, σ_s/c', as a function of three variables:

$$[1] \qquad \sigma_s/c' = f(\phi',\ \gamma B/c',\ H/B)$$

A continuous loading is applied to the ground surface. Formulating the problem in this manner permits a compact set of stability charts to be constructed, which are useful for practical design purposes. The ranges of problem parameters considered in this paper are for tunnel geometries of $H/B = 1.0 - 5.0$, friction angles of $\phi' = 0°–35°$, and dimensionless unit weights up to $\gamma B/c' = 3.0$, all for which both smooth and rough interface conditions between the loading and soil are considered. To model the smooth interface condition between the loading and the soil, the shear stress is fixed to zero ($\tau = 0$) along the ground surface in the lower bound analyses, with no velocity constraints being imposed in the upper bound analyses. For the rough case, the horizontal velocity is fixed to zero ($u = 0$) along the ground surface in the upper bound analyses, with no stress constraints being imposed in the lower bound analyses.

Numerical limit analysis

Limit analysis utilizes the power of lower and upper bound theorems of plasticity theory to provide rigorous bounds on collapse loads from both below and above. The theorems themselves are based on the principle of maximum power dissipation, which is valid for soil following an associated flow rule. The use of finite element discretization of the soil combined with mathematical optimization to maximize lower bound and minimize upper bound makes it possible to handle routine problems with complex geometries and loading con-

Fig. 1. Plane strain square tunnel in cohesive–frictional soil.

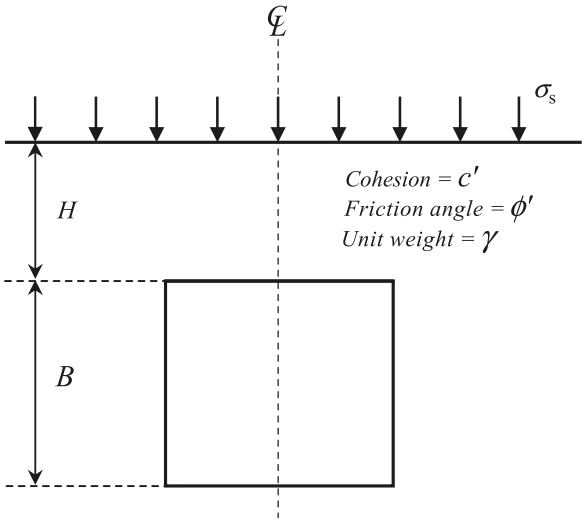

Fig. 2. Typical finite element meshes for a square tunnel ($H/B = 3$, rough interface): (*a*) lower bound mesh; (*b*) upper bound mesh. σ_n, normal stress.

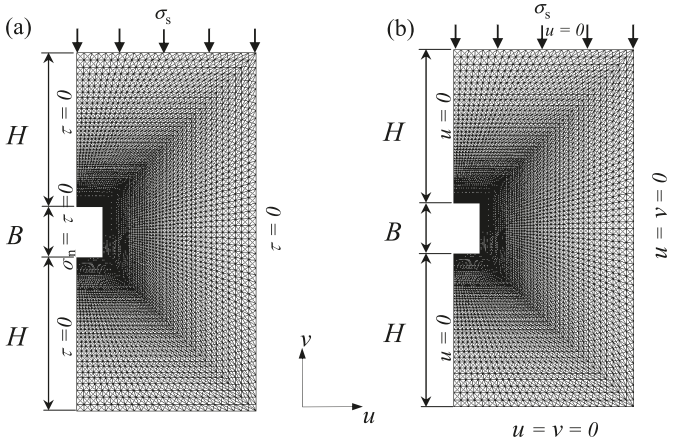

ditions. The formulations of numerical limit analysis used in this paper originate from those given by Sloan (1988, 1989) and Sloan and Kleeman (1995) who employed active set linear programming and discontinuous stress and velocity fields to solve a variety of stability problems. Since then, numerical limit analysis has evolved significantly, and the techniques used in this paper are those described in Lyamin and Sloan (2002) and Krabbenhøft et al. (2005).

In brief, these formulations use linear stress (lower bound) and linear velocity (upper bound) triangular finite elements to discretize the soil mass. In contrast to conventional displacement finite element analysis, each node in the limit analysis mesh is unique to a particular element so that statically admissible stress (LB) and kinematically admissible velocity discontinuities (UB) are permitted to occur along shared edges between two adjacent elements. The objective of the lower bound analysis is to maximize the load multiplier subject to element equilibrium, stress boundary conditions, and yield constraints. For the upper bound analysis, the internal power dissipation less the rate of work done by prescribed external forces is minimized subject to velocity boundary conditions, compatibility, and flow rule constraints. Both formulations result in convex mathematical programs, which (considering the dual form of upper bound problem) can be cast in the following form:

$$\begin{aligned} &\text{Maximize} && \lambda \\ &\text{subject to} && \mathbf{A}\boldsymbol{\sigma} = \boldsymbol{p}_0 + \lambda \boldsymbol{p} \\ & && f_i(\boldsymbol{\sigma}) \le 0, \quad i = (1, \ \ldots, \ N) \end{aligned} \tag{2}$$

where λ is a load multiplier, $\boldsymbol{\sigma}$ is a vector of stress variables, $\mathbf{A}$ is a matrix of equality constraint coefficients, $\boldsymbol{p}_0$ and $\boldsymbol{p}$ are vectors of prescribed and optimizable forces, respectively, f_i is the yield function for stress set i, and N is the number of stress nodes.

The solution to the above optimization problem can be found efficiently by solving the system of nonlinear equations that define its Kuhn–Tucker optimality conditions. The interior point procedure used is based on a two-stage quasi Newton algorithm, requires usually 30–50 iterations, regardless of the problem size, and is many times faster than previously employed linear programming schemes. The solutions of the lower and upper bound computations bracket the actual collapse load from below and above, and thus give a clear indication of the accuracy of the results.

Figures 2*a* and 2*b* show the typical lower bound and upper bound half-meshes for $H/B = 3$, with rough interfaces. The meshes are symmetric, and similar meshes are used for lower and upper bound analyses. The lower and upper bound meshes have 20 000 triangular elements and 29 850 stress and velocity discontinuities. In the lower bound analysis, special extension elements are included along the soil domain boundaries to represent a semi-infinite material. This feature is necessary to guarantee that the lower bounds are fully rigorous, and is a convenient means of extending the stress field throughout a semi-infinite domain in a manner that satisfies equilibrium, the stress boundary conditions, and the yield criterion. The size of the soil domain for each of the tunnel geometries considered is chosen such that the plasticity zone at failure lies well inside the domain. Careful mesh refinement is required to obtain accurate solutions, with the mesh density being high around the tunnel face, with a smooth transition to larger elements near the boundary of the mesh.

Upper bound rigid-block analysis

Semi-analytical rigid-block mechanisms were also used in this study to model the upper bound stability of the tunnel. These provided an additional check on the solutions obtained using numerical limit analysis and have been developed to serve as simple design tools for practicing engineers. The four rigid-block mechanisms considered are shown in Fig. 3 and model failure of the tunnel in a range of modes from a simple trapdoor failure, usually associated with the failure of very shallow tunnels, failure modes with roof and side collapse, and a mechanism that also exhibits base heave that is typical of deeper tunnels. In Fig. 3, A_i is the area of rigid-block i; V_i is the kinematically admissible velocity of the rigid block; V_{ij} is the velocity jump along the discontinuity between blocks i and j; l_{ij} is the distance of segment between

blocks i and j; s is the width of ground surface subjected to surcharge, σ_s; α, β, γ, δ, and ε are the unknown angular parameters that determine the geometry of rigid-block mechanisms; ϕ' is the friction angle; and ω is the known angular parameter. The compatible velocity diagrams using V_i and V_{ij} are given at the right side of the block mechanisms. All velocities can be obtained using the geometry of these diagrams. With an associated flow rule, we assume the dilatancy angle is equal to the friction angle. Although it is well known that the use of an associated flow rule predicts excessive dilation during shear failure of frictional soils, it is unlikely this feature will have a major impact on the predicted limit loads for cases with low to moderate friction angles. Generally speaking, any inaccuracy caused by an associated flow rule will be most pronounced for soils with very high friction angles and (or) problems that are subject to high degrees of kinematic constraint (which is not the case for the tunnels considered here). The soil mass is assumed to be governed by the Mohr–Coulomb failure criterion and an associated flow rule. The geometry of rigid blocks is allowed to vary while being constrained such that the areas of the rigid blocks and lengths of the boundary segments stay positive. The details of rigid-block analysis can be found in Chen (1975). The upper bound solutions derived from mechanisms 1–4 are given as follows:

Mechanism 1:

$$[3] \qquad \sigma_s \le \frac{c' l_{10}\cos\phi' - A_1\gamma}{s} = \frac{c'H - A_1\gamma}{s}$$

Mechanism 2:

$$[4] \qquad \sigma_s \le \frac{c'\cos\phi'(V_1 l_{10} + V_2 l_{20} + V_{21} l_{12}) - \gamma[A_1 V_1 + A_2 V_2 \sin(\gamma - \phi')]}{sV_1}$$

Mechanism 3:

$$[5] \qquad \sigma_s \le \frac{c'\cos\phi'(V_1 l_{10} + V_2 l_{20} + V_{21} l_{12} + V_3 l_{30} + V_{32} l_{23}) - \gamma[A_1 V_1 + A_2 V_2 \sin(\varepsilon - \phi') - A_3 V_3 \sin(\phi' + \delta)]}{sV_1}$$

Mechanism 4:

$$[6] \qquad \sigma_s \le \frac{c'\cos\phi'(V_2 l_{20} + V_{21} l_{12} + V_3 l_{30} + V_{31} l_{13}) - \gamma[A_1 V_1 + A_2 V_2 \sin(\delta - \phi') + A_3 V_3 \sin(\alpha - \phi')]}{sV_2 \sin(\delta - \phi')}$$

The minimum upper bound solution for each mechanism was obtained by optimizing its geometry by the Hooke and Jeeves algorithm with discrete steps (Bunday 1984). This method works by performing two different types of searches: an exploratory search and a pattern search. The rigid-block analyses are extremely quick, taking the order in just 1 s. Provided an appropriate mechanism is chosen, this technique gives a fairly accurate upper bound estimate that can be used to check the finite element solutions.

Table 1 shows the comparison of upper bound solutions obtained using each mechanism for $H/B = 1.0$–3.0, $\phi' = 0°$–$20°$, and $\gamma B/c' = 0.0$–3.0. It was found that the best solutions (highlighted in bold) were obtained from mechanisms 2 and 4 except for the cases of $H/B = 1.0$, $\phi' = 0°$–$10°$, and $\gamma B/c' = 0.0$–1.0. The quality of solutions from different mechanisms decreases in the following order: mechanism 2, mechanism 4, mechanism 3, and mechanism 1. Mechanism 2 provides better solutions than mechanism 4 for $H/B = 1.0$, $\phi' = 0°$–$10°$, and $\gamma B/c' = 0$–1, but mechanism 4 gives better results for $H/B = 1.0$, $\phi' = 0°$–$10°$, and $\gamma B/c' = 2$ and 3. Among all mechanisms considered, only mechanism 4 was able to provide solutions for deep cases with high friction angles. On the contrary, mechanism 1 was found to be robust only for cases of $H/B = 1.0$, $\phi' = 0°$–$10°$ and $\gamma B/c' = 0$–1. This can be explained by noting that this is a single roof collapse mechanism limited to the cases of very shallow tunnels and low soil frictional angles. Thus, the best upper bound solutions are given by mechanisms 2 and 4, which are composed of two and three rigid blocks, and four and three angular parameters, respectively. The upper bound rigid-block solutions are compared next with the results from numerical limit analysis.

Results and discussion

Figures 4–7 show the rigid-block mechanisms in action and the plots of power dissipations, deformed meshes, and plastic zones for square tunnels obtained from numerical upper and lower bound limit analyses. The intensity of power dissipations and plastic zones is shown by the different shades. The values of dimensionless load parameter, σ_s/c', obtained by using both techniques are included in each figure. In this paper, eq. [7] is used to measure the gap between the bounds, and is thus a direct estimate of the error in the solutions.

$$[7] \qquad \pm \text{error}\ (\%) = \pm 100(\text{UB} - \text{LB})/(\text{UB} + \text{LB})$$

Generally, the distributions of power dissipations agree fairly well with those of plastic zones.

It is found from Figs. 4*b* and 4*d* that the slip surfaces originate at the lower and upper corners of the tunnel and then intersect nearby. The major slip surface originating at the lower corner protrudes almost straight to the ground surface due to the very shallow tunnel depth. However, this effect is not so pronounced for the smooth interface condition. Also, it can be noticed that the failure mechanisms of the rigid-block technique agree well with those observed in the plots of power dissipations and plastic zones. Figure 5 shows the case of $H/B = 1$, $\phi' = 20°$, $\gamma B/c' = 1$, when smooth interface conditions are applied. In Figs. 5*b* and 5*d*, the pattern of the

Fig. 3. Upper bound rigid-block mechanisms for a square tunnel: (*a*) mechanism 1; (*b*) mechanism 2; (*c*) mechanism 3; (*d*) mechanism 4.

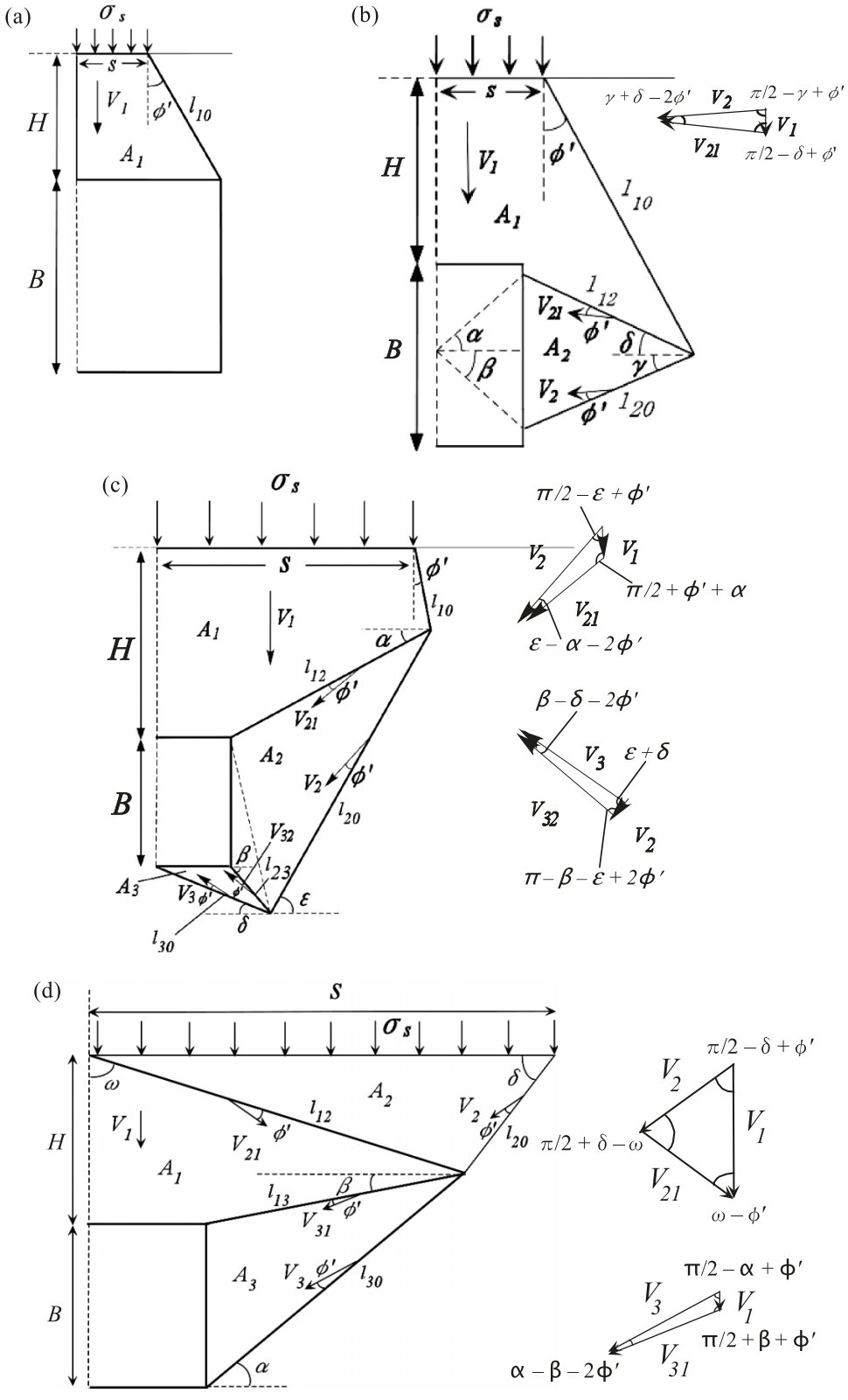

slip surfaces is almost the same as seen in Figs. 4*b* and 4*d*, although a different friction angle is used here. As expected for larger friction angles, the ultimate surcharge load is higher than those presented in Fig. 4. For shallow tunnels ($H/B = 1$) shown in Figs. 4 and 5, the effect of collapsing from the side of the tunnel is not very remarkable. Looking at the power dissipations (Figs. 4*b*, 5*b*, 6*b*, 7*b*) and the plastic zones (Figs. 4*d*, 5*d*, 6*d*, 7*d*), it can be observed that due to

Table 1. Comparison of upper bound values from various rigid-block mechanisms.

H/D	ϕ' (°)	$\gamma D/c' = 0$	$\gamma D/c' = 1$	$\gamma D/c' = 2$	$\gamma D/c' = 3$	$\gamma D/c' = 0$	$\gamma D/c' = 1$	$\gamma D/c' = 2$	$\gamma D/c' = 3$
		Mechanism 1				**Mechanism 2**			
1	0	**2.00**	1.50	1.00	0.50	**2.00**	**1.00**	0.00	–1.00
	5	**2.42**	**1.32**	0.21	–0.89	**2.42**	**1.32**	0.21	–0.89
	10	**3.09**	**1.82**	0.54	–0.73	**3.09**	**1.82**	0.54	–0.73
	15	4.31	2.73	1.15	–0.42	**4.25**	**2.66**	**1.07**	**–0.52**
	20	7.35	5.01	2.68	0.34	**5.68**	**3.86**	**2.03**	**0.20**
2	0	4.00	3.00	2.00	1.00	**3.20**	**0.89**	**–1.43**	**–3.76**
	5	6.15	3.62	1.08	–1.46	**4.06**	**1.53**	**–1.00**	**–3.53**
	10	13.57	9.18	4.79	0.39	**5.48**	**2.60**	**–0.29**	**–3.19**
	15	—	—	—	—	**8.20**	**4.69**	**1.12**	**–2.53**
	20	—	—	—	—	**14.93**	**10.06**	**5.00**	**–0.46**
3	0	6.00	4.50	3.00	1.50	**3.92**	**0.58**	**–2.76**	**–6.10**
	5	12.63	7.97	3.31	–1.34	**5.31**	**1.55**	**–2.22**	**–5.99**
	10	—	—	—	—	**7.97**	**3.44**	**–1.17**	**–5.91**
	15	—	—	—	—	14.62	**8.42**	**1.88**	**–5.90**
	20	—	—	—	—	**44.97**	**33.32**	**20.72**	**5.01**
		Mechanism 3				**Mechanism 4**			
1	0	2.62	1.36	0.08	–1.25	2.36	1.08	**–0.20**	**–1.50**
	5	3.17	1.84	0.50	–0.86	2.78	1.44	**0.09**	**–1.27**
	10	3.96	2.52	1.08	–0.36	3.37	1.93	**0.48**	**–0.96**
	15	5.17	3.59	2.00	0.41	**4.25**	**2.66**	**1.07**	**–0.52**
	20	7.27	5.44	3.61	1.78	**5.68**	**3.86**	**2.03**	**0.20**
2	0	3.50	1.18	–1.17	–3.57	**3.20**	**0.89**	**–1.43**	**–3.76**
	5	4.54	2.01	–0.54	–3.10	**4.06**	**1.53**	**–1.00**	**–3.53**
	10	6.28	3.39	0.49	–2.42	**5.48**	**2.60**	**–0.29**	**–3.19**
	15	9.68	6.18	2.62	–1.03	**8.20**	**4.69**	**1.12**	**–2.53**
	20	18.29	13.54	8.61	3.35	**14.93**	**10.06**	**5.00**	**–0.46**
3	0	4.23	0.85	–2.56	–6.00	**3.92**	**0.58**	**–2.76**	**–6.10**
	5	5.81	2.03	–1.76	–5.56	**5.31**	**1.55**	**–2.22**	**–5.99**
	10	8.85	4.35	–0.23	–4.93	**7.97**	**3.44**	**–1.17**	**–5.91**
	15	16.24	10.36	4.14	–2.88	**14.61**	**8.42**	**1.88**	**–5.90**
	20	45.77	36.55	26.49	14.93	**44.97**	**33.32**	**20.72**	**5.01**

Fig. 4. Comparison of rigid-block mechanism with numerical limit analysis for a square tunnel ($H/B = 1$, $\phi' = 5°$, $\gamma B/c' = 1$, smooth interface): (*a*) rigid-block mechanism; (*b*) power dissipation; (*c*) deformed mesh; (*d*) plastic zones.

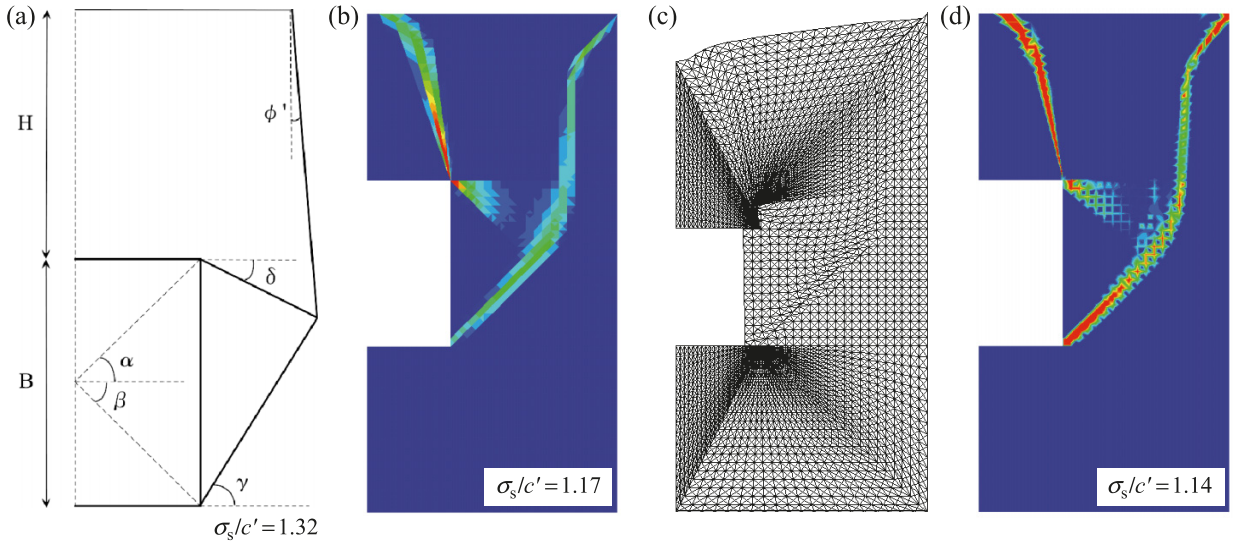

the points of singularity (corners) of tunnel shape not all the area around the tunnel becomes plastic. In all Figs. 4–7, it is noticeable that the areas of intense power dissipations and plastic zones originate at corners and do not actually touch the sides of the tunnel. For the case of $H/B = 1.0$ shown in Figs. 4*c* and 5*c*, the roof of the tunnel collapses down as a

Fig. 5. Comparison of rigid-block mechanism with numerical limit analysis for a square tunnel ($H/B = 1$, $\phi' = 20°$, $\gamma B/c' = 1$, smooth interface): (*a*) rigid-block mechanism; (*b*) power dissipation; (*c*) deformed mesh; (*d*) plastic zones.

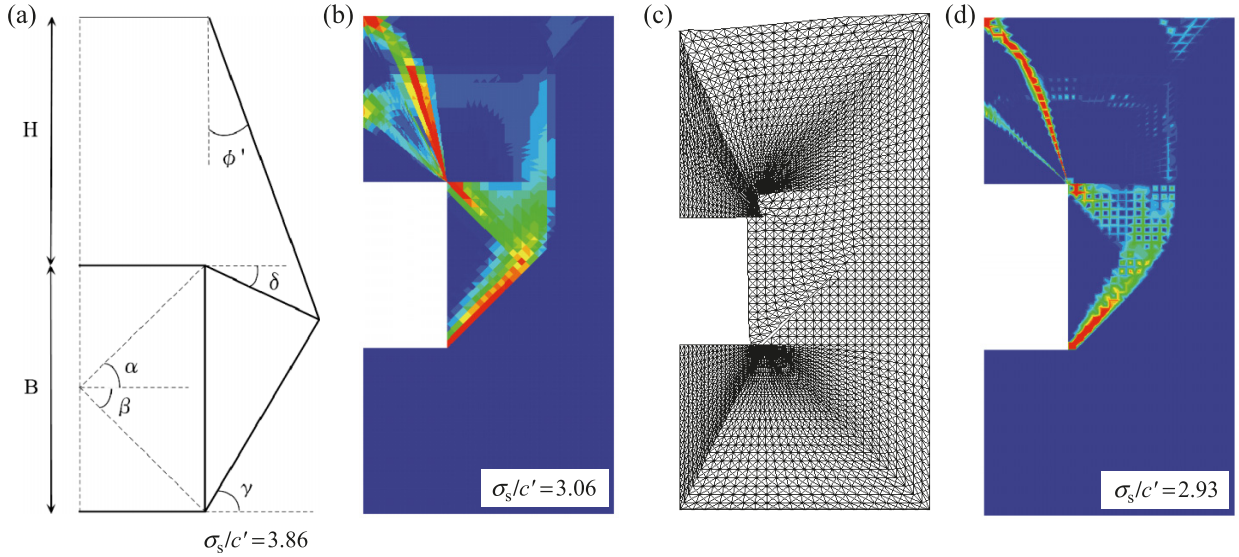

Fig. 6. Comparison of rigid-block mechanism with numerical limit analysis for a square tunnel ($H/B = 2$, $\phi' = 15°$, $\gamma B/c' = 1$, smooth interface): (*a*) rigid-block mechanism; (*b*) power dissipation; (*c*) deformed mesh; (*d*) plastic zones.

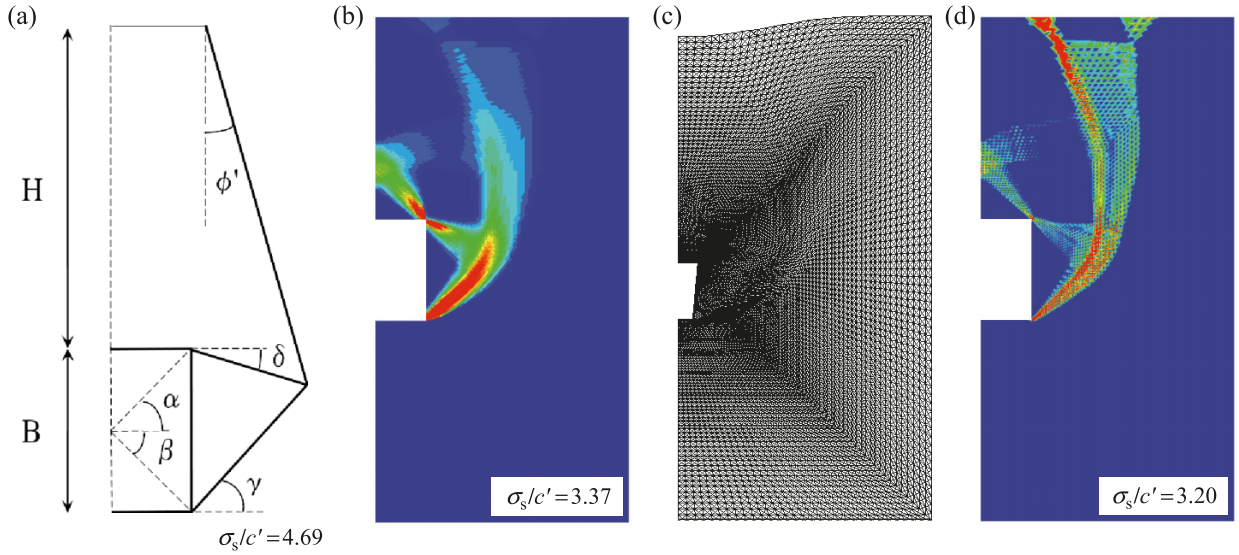

rigid block, and the failure area extends right to the surface (Fig. 4*c*). When H/B is increased as shown in Figs. 6 and 7, the major slip surface originating at the lower corner of the tunnel curves more toward the ground surface, and the effect of collapsing from the side of the tunnel becomes more noticeable, especially for moderate values of friction angle. Also, as seen in Figs. 7*b*–7*d*, these deeper collapse mechanisms are more complex than those for shallower tunnels. The errors calculated by eq. [7] in the cases shown in Figs. 4–7 are 1.3%, 2.2%, 2.6%, and 17.6%, respectively. The high value of error in the last case is explained by the fact that the stability numbers are close to zero for the problem parameters considered therein, making it hard to keep the relative error at a low level.

The rigorous lower and upper bound solutions bracket the true ultimate surcharge load quite accurately for the case of moderate frictional angles. As was mentioned before, of all the developed rigid-block mechanisms shown in Fig. 3, the best upper bound solutions for most cases were obtained using mechanisms 2 and 4. Thus, it can be concluded that the collapse mechanisms, which accounts for both the roof and the side failures, are most efficient for the case of square tunnels. In general, the upper bound solutions obtained from the rigid-block and the numerical limit analyses are in a good agreement; however, the rigid-block results tend to be larger than the limit analysis values, especially when H/B or ϕ' increases. This is due to deeper tunnels, which have a more complex collapse pattern; therefore, the simple rigid-block

Fig. 7. Comparison of rigid-block mechanism with numerical limit analysis for a square tunnel ($H/B = 4$, $\phi' = 5°$, $\gamma B/c' = 1$, smooth interface): (*a*) rigid-block mechanism; (*b*) power dissipation; (*c*) deformed mesh; (*d*) plastic zones.

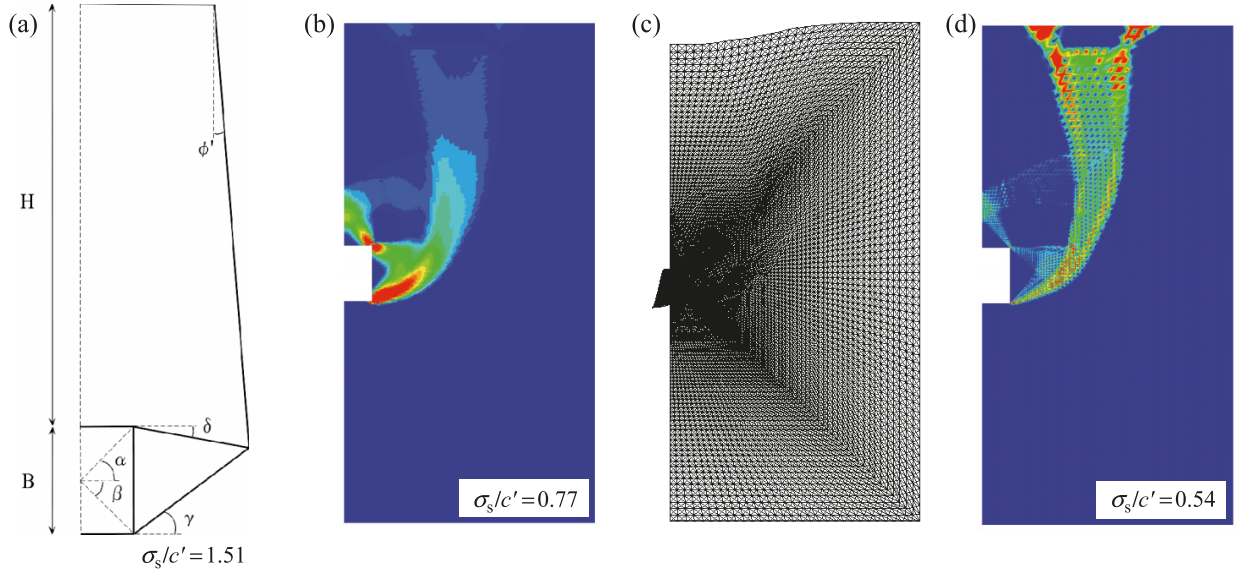

Fig. 8. Numerical limit analysis for a circular tunnel ($H/D = 1$, $\phi' = 5°$, $\gamma D/c' = 1$, smooth interface): (*a*) power dissipation; (*b*) deformed mesh; (*c*) plastic zones.

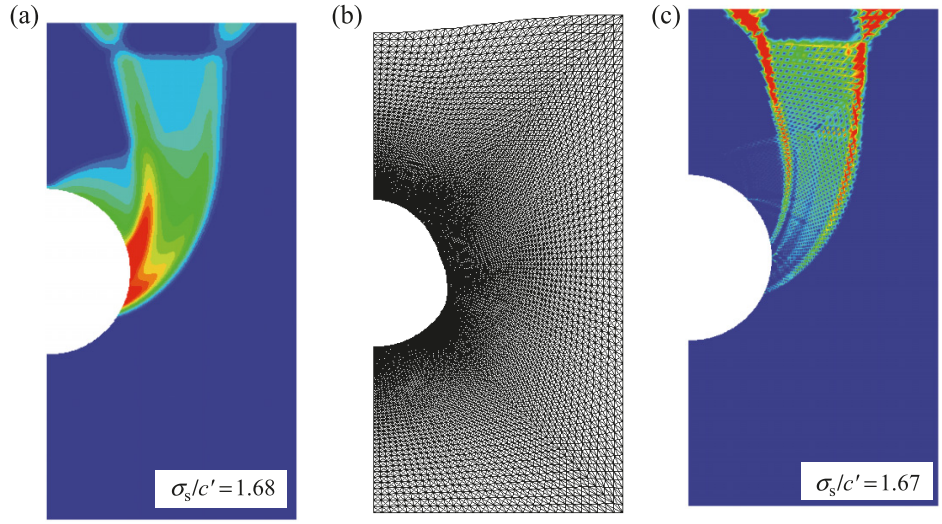

mechanisms proposed are generally less accurate for such geometries. Furthermore, it is more difficult to propose an efficient rigid-block mechanism in the case of cohesive–frictional soils where nonzero normal velocity jumps across interblock discontinuity must be accounted for. Therefore, even using best-performing mechanisms 2 and 4, the feasible solutions could not be easily obtained for high values of H/B or ϕ'.

For the sake of comparison, the plots of power dissipations, deformed meshes, and plastic zones for a circular tunnel are shown in Figs. 8 and 9 for the same geometric and soil parameters as those presented in Figs. 4 and 5 for square tunnels. Comparing these plots, it can be observed that the failure mechanism of shallow circular tunnels is quite different to the cases of shallow square tunnels. As expected, the ultimate surcharge loads for circular tunnels are higher than those for square tunnels due to the better stress distribution around a circular tunnel known as "arching effect".

The detailed centrifuge experiments conducted by Mair (1979) provide an opportunity to compare observed behavior against the predictions of numerical limit analysis. Some of Mair's results, for the case of circular tunnel, zero friction angle ($\phi' = 0°$), no surcharge, and a uniform undrained shear strength (c_u), are shown in Fig. 10. Here, H is tunnel depth, D is tunnel diameter, σ_t is internal tunnel pressure, and γ is soil unit weight. As expected, the plots of stability numbers for the square tunnels are located below the corresponding plots for the circular tunnels for all ranges of H/D (H/B). The stability bounds for the circular tunnels (obtained here for the purpose of comparison) have almost coincident LB and UB plots and are in excellent agreement with the experimental observations, which show surprisingly little scatter.

Figure 11 shows the stability numbers obtained from both the rigid-block and numerical limit analyses. The interface condition is smooth, and the results from the rigid-block

Fig. 9. Numerical limit analysis for a circular tunnel ($H/D = 1$, $\phi' = 20°$, $\gamma D/c' = 1$, smooth interface): (*a*) power dissipation; (*b*) deformed mesh; (*c*) plastic zones.

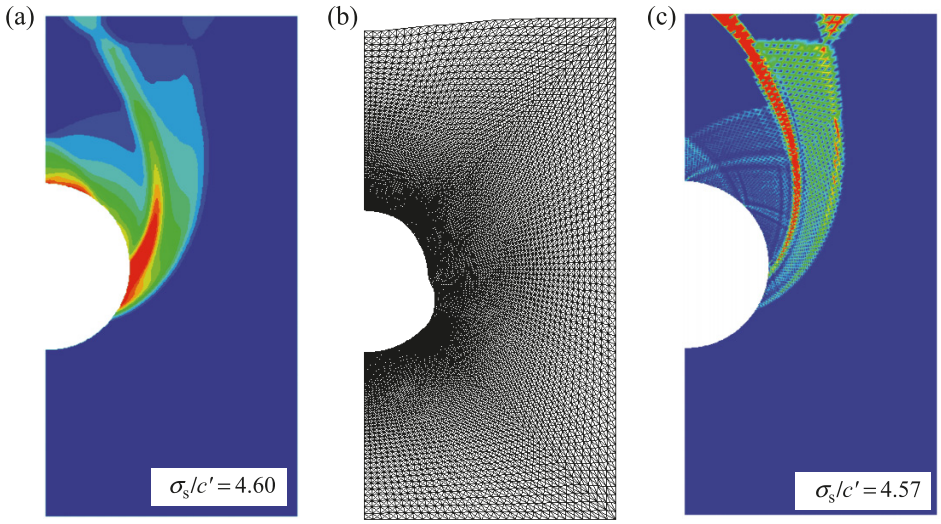

Fig. 10. Comparison of results with published data for a shallow circular tunnel in soil with uniform undrained shear strength ($\gamma D/c_u = 2.6$).

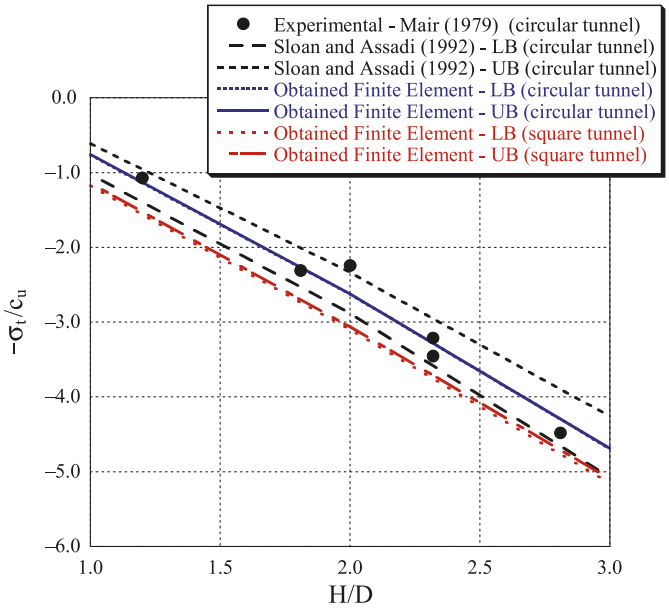

analyses are shown for friction angles up to 20°. The lower and upper bound solutions of the numerical limit analysis for each $\gamma B/c'$ are plotted using broken and solid lines, respectively, and it can be noticed that they bracket the true ultimate surcharge load very accurately for small friction angles, ϕ'. As a general trend for all considered cases, stability numbers decrease when $\gamma B/c'$ increases. Starting from $\phi' = 30°$ (Fig. 11*d*), the ultimate surcharge load increases considerably with the increase of H/B. The plots in Fig. 11 demonstrate that for the cases of Fig. 11*a* where $\phi' = 5°$, $H/B \leq 5$, Fig. 11*b* where $\phi' = 10°$, $H/B \leq 3$, and Fig. 11*c* where $\phi' = 20°$, $H/B \leq 1$, the upper bound solutions from the rigid-block method have relatively good agreement with those obtained from the numerical limit analysis. But for the cases of high H/B or ϕ', the accuracy of considered rigid-block mechanisms becomes poor. In most cases of $\gamma B/c' = 3$ and $H/B \geq 3$, shown in Figs. 11*b* and 11*c*, the feasible solutions from the rigid-block and numerical limit analyses could not be obtained because the tunnel collapses under soil self weight. It is important to mention the sign convention used for stability numbers presentation. A positive value of stability number implies that a compressive normal stress can be applied to the ground surface up to this value, while a negative stability number means that we can only apply a tensile normal stress to the soil surface (no surcharge load in normal sense). The negative range of stability numbers is likely to be of less practical interest.

Figure 12 presents stability numbers obtained by numerical limit analysis for a surface loading with a rough interface. For this condition, the overall trend in the solutions appears similar to results of the smooth case but with ultimate surcharge loads are slightly higher. For most cases shown in Figs. 11 and 12, it can be stated that the rigorous lower and upper bounds accurately bracket the true ultimate surcharge load, except for the particular cases of deeper tunnels and high friction angles ($H/B = 4$ and 5, $\phi' = 30°$) where there is a large difference between the bounds.

Finally, based on the results obtained, an empirical expression that approximates the ultimate surcharge loading of cohesive–frictional soils with the inclusion of shallow square tunnels has been proposed as follows:

$$[8] \quad \sigma_s/c' = [a + \exp(b\phi'^c)](H/B)^{d\exp(e\phi'^f)}[1 + (g + h\phi')(H/B)^{(k+m\phi')}(\gamma B/c')]$$

This parametric equation is a function of two dimensionless variables, H/B and $\gamma B/c'$, and the soil friction angle, ϕ'. The regression coefficients, a, b, c, d, e, f, g, h, k, and m, are obtained by least-squares fit, considering all range of results, so that eq. [8] best approximates the average value between the lower and upper bound solutions. It should be noted that this equation is not related to the traditional bearing capacity equation, that is, eq. [8] is not supposed to converge to a bearing capacity of a footing of a finite size as H/D tends to

Fig. 11. Stability bounds for a square tunnel (smooth interface): (*a*) $\phi' = 5°$; (*b*) $\phi' = 10°$; (*c*) $\phi' = 20°$; (*d*) $\phi' = 30°$.

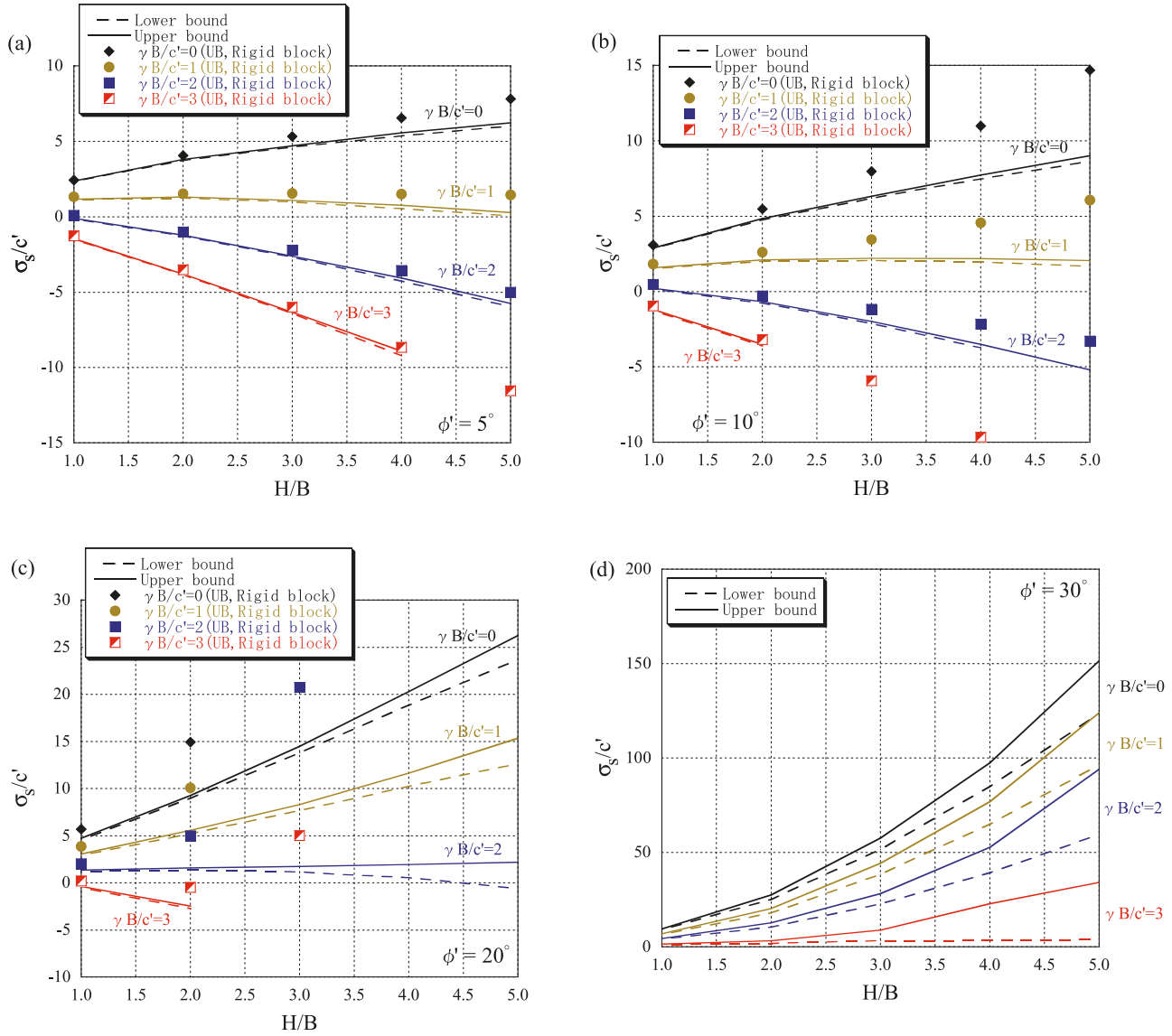

infinity. The bearing capacity of the footing of a finite size is associated with classical Prandtl or Hill collapse mechanisms around the footing. The collapse of the tunnel or opening due to the stress distribution induced by continuous surcharge (infinite length) is associated with absolutely different mechanisms (Figs. 4–9). The switch between different collapse mechanisms could be a part of discussions if the length of surcharge application would be a problem parameter, but this would be a topic for a separate study, as the relative position of the loaded surface segment (rigid or flexible) with respect to the tunnel would then need to be considered as well. Table 2 provides values of regression constants for both smooth and rough interface conditions, and Tables 3 and 4 show the comparison of the average values from numerical limit analysis with those obtained from the presented empirical equation. As can be seen from these tables, the stability number σ_s/c' calculated using the empirical equation follows the average value of numerical solutions quite accurately. Moreover, the developed equation covers all range of considered H/B and ϕ', with the average accuracy being around 7.5% for smooth and 8.5% for rough interfaces, which is considered to be appropriate for engineering practice. Thus, eq. [8] provides a simple complementary option (apart from stability charts) for design engineers, as the ultimate surcharge load of cohesive–frictional soils with inclusion of shallow square tunnels can be readily computed without the need for complicated numerical analyses.

Conclusions

The stability of a plane strain square tunnel, in a cohesive–frictional soil subjected to surcharge loading, has been investigated analytically and numerically. The results of these analyses have been presented in the form of dimensionless stability charts. The lower and upper bounds obtained using numerical limit analysis bracket the actual ultimate surcharge

Fig. 12. Stability bounds for a square tunnel ($\phi' = 5°$, 10°, 20°, 30°, rough interface): (*a*) $\phi' = 5°$; (*b*) $\phi' = 10°$; (*c*) $\phi' = 20°$; (*d*) $\phi' = 30°$.

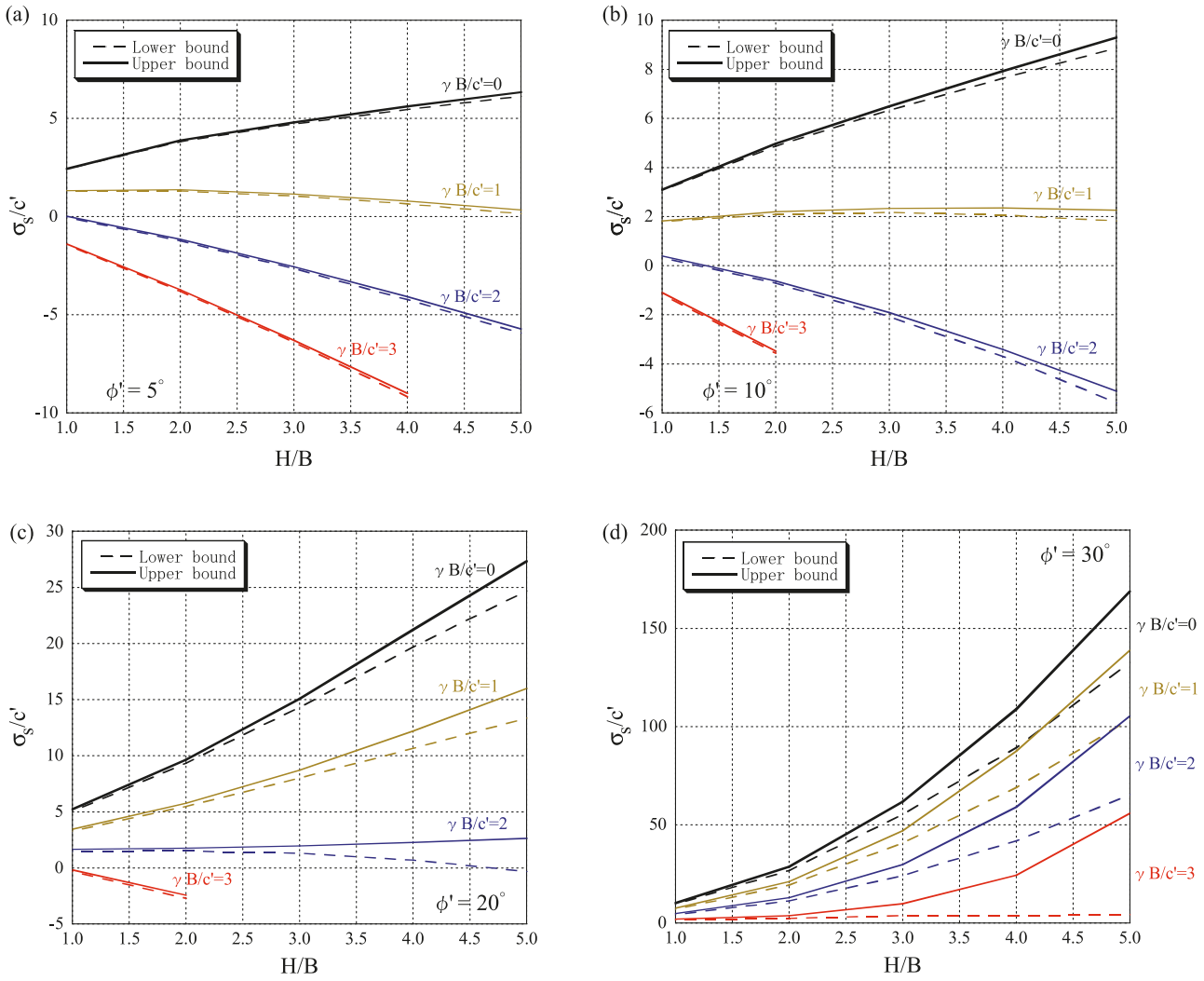

Table 2. Coefficients of empirical equation.

Parameters	Smooth interface	Rough interface
a	1.173 316	1.262 685
b	0.053 366	0.058 050
c	1.055 378	1.048 910
d	0.489 213	0.484 789
e	0.013 242	0.011 488
f	1.349 411	1.387 802
g	–0.564 943	–0.547 691
h	0.009 707	0.009 348
k	0.444 841	0.441 574
m	–0.013 804	–0.012 305

load to within ±10% or better for the range of moderate tunnel depths and soil friction angles. Several rigid-block mechanisms for square tunnels have been developed to check the validity of numerical limit analysis and serve as a handy practical means for geotechnical practitioners. Comparison of upper bound solutions obtained from the rigid-block analyses with those of the numerical limit analyses shows a good agreement when ϕ' and *H*/*B* are small. It is found that the failure mechanisms of shallow square tunnels are quite different to the cases of shallow circular tunnels due to the absence of the significant arching effect present in the latter cases. As expected, the ultimate surcharge loads for square tunnels are always lower than those for circular tunnels. An empirical equation for estimating the ultimate surcharge load of cohesive–frictional soils with inclusion of shallow square tunnels has been proposed, which is based on the average values between the lower and upper bounds from numerical limit analysis. The presented equation has the average accuracy of 7.5% for smooth and 8.5% for rough interfaces, which is considered to be suitable for engineering practice. For future work, it is proposed that the tunnels or openings of shapes other than circular and square will be considered, and more accurate rigid-block mechanisms better suited for high frictional angles will be developed.

Table 3. Comparison of average values from numerical limit analysis with those obtained from empirical equation (smooth interface).

		(LB + UB)/2				Empirical equation			
ϕ' (°)	H/B	$\gamma B/c' = 0$	$\gamma B/c' = 1$	$\gamma B/c' = 2$	$\gamma B/c' = 3$	$\gamma B/c' = 0$	$\gamma B/c' = 1$	$\gamma B/c' = 2$	$\gamma B/c' = 3$
0	1	1.96	0.88	–0.36	–1.69	2.17	0.95	–0.28	–1.51
	2	3.05	0.73	–1.64	–4.04	3.05	0.70	–1.64	–3.99
	3	3.64	0.32	–3.06	–6.51	3.72	0.29	–3.13	–6.56
	4	4.13	–0.20	–4.59	–9.11	4.28	–0.20	–4.68	–9.16
	5	4.52	–0.82	–6.25	–11.80	4.78	–0.74	–6.27	–11.79
5	1	2.36	1.16	–0.13	–1.47	2.51	1.21	–0.08	–1.38
	2	3.76	1.27	–1.25	–3.82	3.68	1.21	–1.25	–3.71
	3	4.66	1.03	–2.64	–6.38	4.59	1.01	–2.58	–6.16
	4	5.46	0.66	–4.17	–9.06	5.38	0.70	–3.98	–8.65
	5	6.11	0.16	–5.87	—	6.08	0.33	–5.42	–11.17
10	1	2.87	1.55	0.19	–1.22	3.01	1.60	0.19	–1.21
	2	4.79	2.06	–0.72	–3.56	4.74	2.00	–0.75	–3.49
	3	6.25	2.14	–2.04	—	6.19	2.13	–1.93	–5.98
	4	7.60	2.07	–3.61	—	7.48	2.13	–3.23	–8.59
	5	8.83	1.88	NA	—	8.67	2.02	–4.62	–11.27
15	1	3.59	2.13	0.63	–0.90	3.71	2.15	0.60	–0.96
	2	6.41	3.29	0.10	–3.19	6.53	3.30	0.07	–3.16
	3	8.96	4.10	–0.94	—	9.09	4.14	–0.81	–5.76
	4	11.54	4.86	–2.28	—	11.49	4.79	–1.91	–8.61
	5	13.97	5.44	NA	—	13.79	5.31	–3.17	–11.64
20	1	4.66	3.00	1.29	–0.46	4.70	2.96	1.21	–0.53
	2	9.13	5.41	1.48	–2.60	9.66	5.63	1.61	–2.42
	3	14.13	7.99	1.45	—	14.73	8.16	1.58	–4.99
	4	19.58	10.94	1.25	—	19.87	10.56	1.25	–8.06
	5	24.96	13.99	0.79	—	25.06	12.87	0.68	–11.52
25	1	6.36	4.38	2.35	0.49	6.10	4.13	2.17	0.20
	2	14.42	9.56	4.46	–1.08	15.61	10.22	4.83	–0.56
	3	25.48	16.91	7.51	—	27.05	17.32	7.60	–2.13
	4	38.06	25.98	11.38	—	39.95	25.17	10.38	–4.40
	5	51.80	36.13	16.12	—	54.07	33.61	13.15	–7.31
30	1	9.22	6.75	4.19	1.40	8.08	5.87	3.66	1.45
	2	26.25	19.18	11.57	2.58	28.18	20.30	12.42	4.54
	3	54.67	41.28	25.38	6.02	58.50	41.94	25.38	8.81
	4	91.16	70.95	46.05	13.18	98.24	70.18	42.12	14.05
	5	137.49	110.09	76.81	18.96	146.86	104.62	62.38	20.14
35	1	14.63	11.23	7.68	3.83	10.89	8.44	5.99	3.53
	2	59.08	46.61	32.79	15.25	58.94	46.01	33.09	20.16
	3	150.83	125.22	92.69	48.85	158.24	124.07	89.90	55.73
	4	309.12	265.79	208.07	122.52	318.87	250.77	182.68	114.58
	5	549.11	482.91	390.56	250.25	549.10	432.84	316.57	200.30

Note: NA, not applicable.

Table 4. Comparison of average values from numerical limit analysis with those obtained from empirical equation (rough interface).

		(LB + UB)/2				Empirical equation			
ϕ' (°)	H/B	$\gamma B/c' = 0$	$\gamma B/c' = 1$	$\gamma B/c' = 2$	$\gamma B/c' = 3$	$\gamma B/c' = 0$	$\gamma B/c' = 1$	$\gamma B/c' = 2$	$\gamma B/c' = 3$
0	1	2.00	1.00	–0.29	–1.65	2.26	1.02	–0.22	–1.46
	2	3.11	0.79	–1.58	–3.98	3.17	0.81	–1.54	–3.90
	3	3.70	0.38	–3.00	–6.44	3.85	0.43	–3.00	–6.43
	4	4.18	–0.05	–4.53	–9.03	4.43	–0.05	–4.52	–9.00
	5	4.63	–0.70	–6.11	–11.68	4.94	–0.57	–6.07	–11.57
5	1	2.43	1.32	–0.01	–1.42	2.63	1.31	0.00	–1.32
	2	3.84	1.34	–1.20	–3.77	3.83	1.33	–1.16	–3.66
	3	4.76	1.10	–2.60	–6.35	4.76	1.14	–2.48	–6.10
	4	5.54	0.72	–4.16	–9.09	5.56	0.84	–3.87	–8.59
	5	6.23	0.25	–5.82	—	6.27	0.48	–5.31	–11.11
10	1	3.08	1.81	0.36	–1.14	3.18	1.73	0.29	–1.15
	2	4.92	2.15	–0.67	–3.53	4.96	2.15	–0.66	–3.47
	3	6.41	2.25	–1.99	—	6.43	2.29	–1.86	–6.00
	4	7.79	2.21	–3.55	—	7.74	2.27	–3.19	–8.66
	5	9.07	2.04	–5.35	—	8.93	2.16	–4.61	–11.38
15	1	4.01	2.46	0.87	–0.76	3.96	2.35	0.73	–0.88
	2	6.60	3.41	0.15	–3.17	6.87	3.53	0.18	–3.17
	3	9.24	4.28	–0.87	—	9.48	4.36	–0.77	–5.89
	4	11.91	5.09	–2.20	—	11.91	4.98	–1.95	–8.88
	5	14.51	5.76	–1.70	—	14.21	5.46	–3.30	–12.06
20	1	5.12	3.36	1.57	–0.26	5.10	3.26	1.42	–0.42
	2	9.48	5.61	1.62	–2.57	10.27	6.03	1.79	–2.46
	3	14.69	8.36	1.64	—	15.47	8.55	1.63	–5.28
	4	20.46	11.42	1.48	—	20.68	10.90	1.12	–8.67
	5	26.01	14.67	1.15	—	25.91	13.11	0.31	–12.50
25	1	6.85	4.77	2.66	0.49	6.73	4.62	2.50	0.39
	2	15.05	9.97	4.65	–1.12	16.79	11.00	5.22	–0.56
	3	26.79	17.77	7.98	—	28.65	18.23	7.81	–2.62
	4	40.43	27.73	12.43	—	41.87	26.04	10.21	–5.62
	5	55.12	38.76	17.83	—	56.20	34.31	12.42	–9.47
30	1	9.85	7.23	4.54	1.74	9.08	6.66	4.23	1.80
	2	27.68	20.14	12.05	2.99	30.74	22.10	13.46	4.83
	3	58.47	43.87	26.95	6.75	62.73	44.58	26.42	8.27
	4	99.07	78.21	50.40	14.08	104.05	73.31	42.56	11.82
	5	150.73	121.29	85.31	30.05	154.07	107.80	61.54	15.28
35	1	15.78	12.13	8.32	4.23	12.48	9.73	6.98	4.22
	2	62.86	49.23	34.13	16.58	65.52	50.96	36.41	21.85
	3	162.75	135.66	99.86	53.46	172.83	134.26	95.69	57.12
	4	329.72	288.95	218.46	132.60	343.94	266.94	189.95	112.95
	5	586.47	513.83	413.85	270.96	586.55	454.92	323.30	191.67

References

Assadi, A., and Sloan, S.W. 1991. Undrained stability of shallow square tunnel. Journal of Geotechnical Engineering, **117**(8): 1152–1173. doi:10.1061/(ASCE)0733-9410(1991)117:8(1152).

Atkinson, J.H., and Cairncross, A.M. 1973. Collapse of a shallow tunnel in a Mohr–Coulomb material. *In* Proceedings of the Symposium on the Role of Plasticity in Soil Mechanics, Cambridge, UK, 13–15 September 1973. *Edited by* A.C. Palmer. University of Cambridge, Cambridge, UK. pp. 202–206.

Bunday, B.D. 1984. Basic optimisation methods. Edward Arnold Publishers Ltd., London, UK.

Cairncross, A.M. 1973. Deformation around model tunnels in stiff clay. Ph.D. thesis, University of Cambridge, Cambridge, UK.

Chen, W.F. 1975. Limit analysis and soil plasticity. Elsevier, Amsterdam, the Netherlands.

Davis, E.H., Gunn, M.J., Mair, R.J., and Seneviratne, H.N. 1980. The stability of shallow tunnels and underground openings in cohesive material. Géotechnique, **30**(4): 397–416. doi:10.1680/geot.1980.30.4.397.

Krabbenhøft, K., Lyamin, A.V., Hjiaj, M., and Sloan, S.W. 2005. A new discontinuous upper bound limit analysis formulation. International Journal for Numerical Methods in Engineering, **63**(7): 1069–1088. doi:10.1002/nme.1314.

Leca, E., and Dormieux, L. 1990. Upper and lower bound solutions for the face stability of shallow circular tunnels in frictional material. Géotechnique, **40**(4): 581–606. doi:10.1680/geot.1990.40.4.581.

Lyamin, A.V., and Sloan, S.W. 2000. Stability of a plane strain circular tunnel in a cohesive–frictional soil. *In* Proceedings of the Booker Memorial Symposium, Sydney, N.S.W., Australia, 16–17 November 2000. *Edited by* D.W. Smith and J.P. Carter. Balkema, Rotterdam, the Netherlands. pp. 139–153.

Lyamin, A.V., and Sloan, S.W. 2002. Lower bound limit analysis using non-linear programming. International Journal for Numerical Methods in Engineering, **55**(5): 573–611. doi:10.1002/nme.511.

Lyamin, A.V., Jack, D.L., and Sloan, S.W. 2001. Collapse analysis of square tunnels in cohesive–frictional soils. *In* Proceedings of the First Asian–Pacific Congress on Computational Mechanics, Sydney, N.S.W., Australia, 20–23 November 2001. *Edited by* S. Valliappan and N. Khalili. Elsevier, Amsterdam, the Netherlands. pp. 405–414.

Mair, R.J. 1979. Centrifugal modelling of tunnel construction in soft clay. Ph.D. thesis, University of Cambridge, Cambridge, UK.

Muhlhaus, H.B. 1985. Lower bound solutions for circular tunnels in two and three dimensions. Rock Mechanics and Rock Engineering, **18**: 37–52. doi:10.1007/BF01020414.

Seneviratne, H.N. 1979. Deformations and pore-pressures around model tunnels in soft clay. Ph.D. thesis, University of Cambridge, Cambridge, UK.

Sloan, S.W. 1988. Lower bound limit analysis using finite elements and linear programming. International Journal for Numerical and Analytical Methods in Geomechanics, **12**(1): 61–77. doi:10.1002/nag.1610120105.

Sloan, S.W. 1989. Upper bound limit analysis using finite elements and linear programming. International Journal for Numerical and Analytical Methods in Geomechanics, **13**(3): 263–282. doi:10.1002/nag.1610130304.

Sloan, S.W., and Assadi, A. 1991. Undrained stability of a square tunnel in a soil whose strength increases linearly with depth. Computers and Geotechnics, **12**(4): 321–346. doi:10.1016/0266-352X(91)90028-E.

Sloan, S.W., and Assadi, A. 1992. Stability of shallow tunnels in soft ground. *In* Proceedings of the Wroth Memorial Symposium, Oxford, UK, 27–29 July 1992. *Edited by* G.T. Houlsby and A.N. Schofield. Thomas Telford, London, UK. pp. 644–663.

Sloan, S.W., and Kleeman, P.W. 1995. Upper bound limit analysis using discontinuous velocity fields. Computer Methods in Applied Mechanics and Engineering, **127**(1–4): 293–314. doi:10.1016/0045-7825(95)00868-1.

Yamamoto, K., Lyamin, A.V., Sloan, S.W., and Abbo, A.J. 2007. Bearing capacity of a cohesive–frictional soil with a shallow tunnel. *In* Proceedings of the 13th Asian Regional Conference on Soil Mechanics and Geotechnical Engineering, Kolkata, India, 10–14 December 2007. *Edited by* N. Som. Allied Publishers Pvt. Ltd., New Delhi, India. Vol. 1, pp. 489–492.